Dominant Modes of China Summer Heat Waves Driven by Global Sea Surface Temperature and Atmospheric Internal Variability

KAIQIANG DENG

School of Atmospheric Sciences, Sun Yat-sen University, Guangzhou, China

SONG YANG

*School of Atmospheric Sciences, and Guangdong Province Key Laboratory for Climate Change
and Natural Disaster Studies, Sun Yat-sen University, Guangzhou, and Southern Laboratory of Ocean Science
and Engineering, Guangdong, Zhuhai, China*

MINGFANG TING

Lamont–Doherty Earth Observatory, Columbia University, Palisades, New York

PING ZHAO

State Key Laboratory of Severe Weather, Chinese Academy of Meteorological Sciences, Beijing, China

ZUNYA WANG

National Climate Center, China Meteorological Administration, Beijing, China

ABSTRACT

This study applies the maximum temperatures at more than 2000 Chinese stations to investigate the dominant modes of China summer heat waves (HWs). The first empirical orthogonal function (EOF) mode of the HW days reflects an increased frequency of HWs in northern China (NC), while the second and third modes represent two distinct interannual modes, with key regions over the Yangtze River valley (YRV) and southern China (SC), respectively. The NC HWs are possibly associated with the Atlantic–Eurasian teleconnection, showing zonally propagating wave trains over the North Atlantic and Eurasian continent. The YRV HWs are proposed to be linked to the North Atlantic Oscillation, which may trigger a southeastward-propagating wave train over northern Russia and East Asia that results in a high pressure anomaly over the YRV. The SC HWs are obviously dominated by the Indian Ocean and northwest Pacific warm SSTs owing to the transition from the preceding El Niño to La Niña, which excites above-normal highs over SC. The anomalously high pressures over NC, the YRV, and SC are usually accompanied by descending air motions, clear skies, decreased precipitation, and increased solar radiation, which jointly cause a drier and hotter soil condition that favors the emergence of HWs. The GFDL HiRAM experiments are able to reproduce the historical evolution of NC and SC HWs, but fail to capture the YRV HWs. The correlation coefficient between model PC1 (PC2) and observed PC1 (PC3) for the period of 1979–2008 is 0.65 (0.38), which significantly exceeds the 95% (90%) confidence level, indicating that this model has a more faithful representation for the SST-forced HWs.

---

1. Introduction

Heat waves (HWs), characterized by persistent high temperature, are among the most devastating weather events in summer, which may pose huge threats to human health and cause substantial economic losses

(Rey et al. 2009; Coumou and Rahmstorf 2012). In the recent decades, there have been more and more HWs around the world due to the climate change (Meehl and Tebaldi 2004; Deng et al. 2018a,b). For instance, in 2003, an unprecedented HW struck Europe, which led to more than 15 000 deaths in France alone (Fouillet et al. 2006). In 2010, an exceptional HW swept western Russia, which claimed at least 54 000 heat-related deaths (Barriopedro et al. 2011) and caused thousands of wildfires (Konovalov et al. 2011; Witte et al. 2011). In 2013, a record-breaking HW hit eastern China throughout the summer, resulting in a direct economic loss amounting to 59 billion Chinese Yuan (Sun et al. 2014; Zhang et al. 2014) and a total of more than 5758 HW-related illness cases (Gu et al. 2016). The frequency of China HWs has been reported to increase remarkably since the 1990s (Ding et al. 2010; Chen and Zhai 2017) and is projected to further increase in the warming future (Guo et al. 2017), which arouses tremendous interest in the climate community to explore the spatiotemporal variations and physical causes of China HWs.

The mechanisms responsible for the HWs can be generally classified into two types: atmospheric anticyclonic forcing and soil water–surface temperature feedbacks. On the one hand, anticyclonic circulations could reduce cloud cover and increase solar radiation, which induces more diabatic heating at the surface and favors the occurrence of HWs (Dole et al. 2011; Qian et al. 2016; Qian 2017). On the other hand, the deficient soil water in antecedent seasons may strongly reduce evaporation cooling and amplify surface warming, which also alters the low-level conditions in favor of the HWs (Fischer et al. 2007; Hirschi et al. 2011; Stéfanon et al. 2014). In China, HWs are strongly controlled by anticyclonic circulations, but the physical processes associated with the anomalous anticyclones are different from case to case (e.g., Tan et al. 2007; Yang et al. 2013; Zhang et al. 2017; Xia et al. 2018). For example, the unusual highs over southern China (SC) and the Yangtze River valley (YRV) are associated with the displacement of the Pacific subtropical high (Wang et al. 2013; Luo and Lau 2017), the intraseasonal oscillation (Chen and Lu 2015; Chen et al. 2016; Chen and Zhai 2017), and the remote and local forcing of sea surface temperature anomalies (SSTAs) (Hu et al. 2012; Liu et al. 2015), while the abnormal highs over northern China (NC) could result from the western Tibetan Plateau snow cover (Wu et al. 2012, 2016) and the interdecadal modes over the Pacific and Atlantic Oceans (Zhou and Wu 2016).

In the recent years, many studies have tried to make a statistical classification of China HWs, in light of their distinct spatial patterns or significant leading modes, considering that different cases of HWs may involve different physical processes (Wang et al. 2016). Chen et al. (2016) have classified the HWs into two types according to the length of their life cycles (i.e., short-lived and long-lived HWs), which are found to be affected by unique anticyclonic–cyclonic circulations (Chen and Lu 2015). The long-lived HWs in SC are also suggested to be sustained by the transition from El Niño to La Niña (Chen et al. 2018). With a cluster analysis, Wang et al. (2018) have obtained three clusters of China HWs covering southeastern China, NC, and the lower reaches of YRV based on the absolute thresholds. Hu et al. (2017) have further noted that mainland China can be divided into four specific regions based on the leading empirical orthogonal function (EOF) modes of China HWs (i.e., southwest, east, southeast, and northwest), where the northwestern and southeastern regions are the two major domains with most frequent HW activities. Based on an EOF analysis, Wang et al. (2017) have suggested that the first three EOF modes of China HWs reflect the interdecadal, interannual-tripole, and interannual-dipole modes of China HWs, respectively. Nevertheless, the drivers and the physical mechanisms associated with the leading patterns of China HWs are not fully understood. For example, Wang et al. (2017) tended to attribute all of the first three EOF modes of China HWs to the western Pacific SSTAs. However, from Fig. 13a of Wang et al. (2017), significant SSTAs that are related to the first mode are also found in the Atlantic. Besides, SSTAs related to the second mode are hardly seen from their Fig. 13c. That is, other factors in addition to the western Pacific SST, such as the Atlantic SST and the atmospheric internal variability, may also play some role in modulating China HWs.

Therefore, the current study will reexamine the dominant modes of China HWs, focusing on the roles of global SST and atmospheric internal variability in the first three EOF modes of the HWs. The remainder of this paper is organized as follows: The data and method used in this study are described in section 2. The spatiotemporal characteristics of China HWs, including their linear trends and dominant EOF modes, are presented in section 3. Section 4 explores the drivers and the physical mechanisms related to the dominant modes of China HWs, followed by a summary and discussion in section 5.

2. Data and method

a. Datasets

The station data used in this study are the daily maximum temperature (Tmax) values at 2419 meteorological stations within mainland China from 1951 to 2015. This dataset is collected from the China National Stations' Fundamental Elements Datasets V3.0 by the National Meteorological Information Center of the China

Meteorological Administration (CMA) (Cao et al. 2016). According to the CMA classification, the 2419 stations include 212 National Reference Stations, 632 National Basic Stations, and 1575 National Meteorological Observing Stations. Some conventional quality-control procedures, including the checks for climatology, station, and regional outliers and for internal, temporal, and spatial consistency, have been applied to improve the data quality and integrity (Ren et al. 2017). The number of stations has increased rapidly since the 1950s and reached over 2000 in 1961. The datasets are sent to the CMA data center every month after quality and consistency control, which serve as the primary support for operational climate monitoring.

Most stations have a data record longer than 55 years (accounting for 85% of the all stations). To keep a consistent data time period, we ultimately filter 2041 stations where temperature series are available from 1 January 1961 to 31 December 2015 at all sites. Figure 1a shows the geographical distribution of the 2041 stations, which are evenly distributed in eastern China and SC, while the distance among the stations increases in western and northern China. For convenience, the station data are transformed into the $0.5° \times 0.5°$ gridded format using a Cressman interpolation (Cressman 1959). The grid boxes that do not have any stations are set to the locations of missing value (-9.99×10^8).

Additionally, several reanalysis products are applied to diagnose the large-scale conditions associated with the dominant modes of China HWs. The monthly geopotential heights and three-dimensional velocities at multiple levels, the two-layer soil moisture (0–10 cm and 10–200 cm), and the sea level pressure are acquired from the NCEP–NCAR reanalysis (Kalnay et al. 1996), which are with a resolution of $2.5° \times 2.5°$ (T62 Gaussian grid with 192×94 points for the soil moisture) and for the period of 1948–present. In this study, the soil moisture data we analyzed are subtracted from the upper layer, as HWs are more directly associated with the soil moisture at the upper layer rather than in the deeper layers. The monthly Extended Reconstructed Sea Surface Temperature version 4 (ERSSTv4; Huang et al. 2015), which is derived from the International Comprehensive Ocean–Atmosphere Dataset, has a resolution of $2° \times 2°$ and is for the period of 1854–present. The land precipitation datasets are acquired from the Global Precipitation Climatology Centre (GPCC) data (Schneider et al. 2014), calculated from global station data, with a resolution of $0.5° \times 0.5°$ for the period of 1901 to the present. This study also examines the correlations between the dominant modes of China HWs and various atmospheric and oceanic drivers. For example, the North Atlantic Oscillation (NAO) and the Niño-3.4
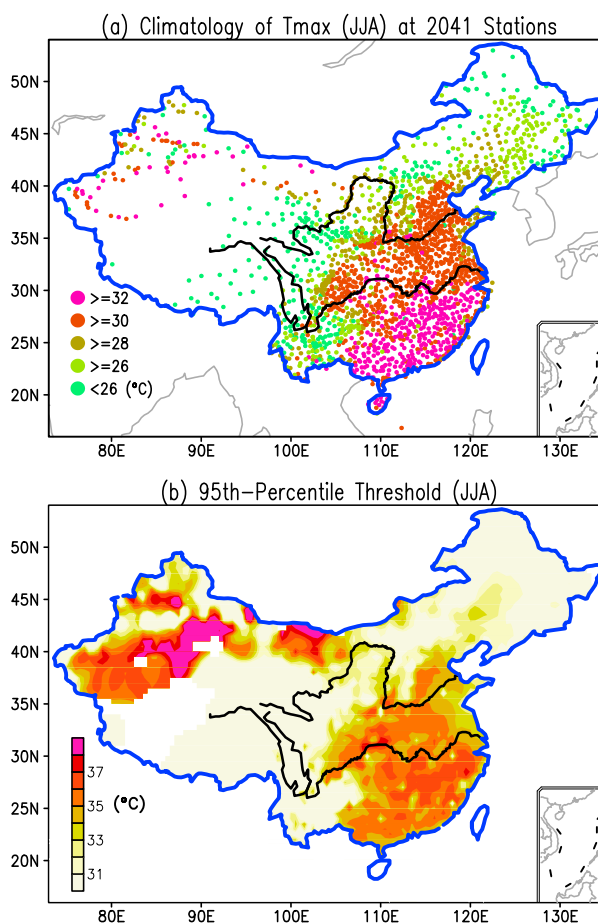

FIG. 1. (a) Climatology of 2-m maximum temperature (Tmax) at 2041 stations averaged from 1 Jun to 31 Aug for all years of 1961–2015. (b) The 95th percentile thresholds of 2-m Tmax, which are similar to (a) except that the station data have been transformed into the $0.5° \times 0.5°$ gridded format. The area lacking the data is not included in the color palette.

index are directly acquired from the website at http://www.esrl.noaa.gov/psd/data/climateindices.

In addition, data from high-resolution atmosphere model (HiRAM) experiments, which were forced by observed SST, are applied to examine the dominant modes of China summer HWs. The model output used in this study includes the daily 2-m surface temperature, geopotential heights, and horizontal winds, at an approximate spatial resolution of 50 km in the horizontal and with 32 levels in the vertical for the period of 1 January 1979–31 December 2008. The HiRAM uses a simpler representation of aerosols than does the Atmospheric Model 3 so that it can run efficiently at higher resolutions (both horizontal and vertical), and uses simplified parameterizations for convection and large-scale cloudiness, with a goal of providing an improved simulation of extreme weather events (Zhao et al. 2009; Harris et al. 2016). The HiRAM experiment is a kind of

AMIP simulation, using the HadISST1 dataset as boundary conditions and producing three ensemble members. All of these simulations include the following changing forcing agents: volcano-generated and anthropogenic aerosols, well-mixed greenhouse gases, prescribed time-varying ozone concentrations, and variations in the incoming solar irradiance. There is no prescribed change in land use. We have calculated the ensemble means for the model before the EOF analysis.

b. Methods

At present, it is hard to obtain a universal definition of HWs (Robinson 2001; Perkins and Alexander 2013). Considering the significant difference in regional climatology, the relative threshold is more meaningful to detect the local extremes in China (Wang et al. 2017). In this study, the China HWs are defined based on a 95th percentile method, which is widely used in previous studies (e.g., Meehl and Tebaldi 2004; Della–Marta et al. 2007; Kuglitsch et al. 2010). For a specific day within June, July, and August (JJA), its Tmax threshold is determined by the 95th percentile of Tmax for a total of 825 days (55 × 15; the 15 days correspond to 7 days on either side of the target date) for the 55 years from 1961 to 2015. By moving the 15-day sampling window forward or backward, we can get a consecutive threshold for every day. An HW event is identified when there are at least 3 consecutive days when the Tmax exceeds its 95th percentile threshold. Therefore, an HW day (HWD) can be acquired by computing the total days during each summer. A larger HWD represents more threshold-breaking hot days or more frequent HWs, and vice versa.

To obtain the dominant modes of China HWs, we conduct an EOF analysis on the China HWD, with an equal area weighting at each grid point by multiplying the square root of the cosine of latitudes due to the decrease in area toward the pole (North et al. 1982). Linear regression/correlation analysis is then performed by regressing/correlating the anomalous atmospheric circulation, SST, and other physical quantities on/with the principal components. It should be noted that assuming the independent samples for individual years for multidecadal SST variability are actually overestimated, it would be better to estimate the effective degrees of freedom based on the method described in the appendix of Metz (1991). In this study, for simplicity, we estimate the effective sample size with the red noise approximation proposed by Zwiers and von Storch (1995):

$$N_{\text{eff}} = N \times (1 - r)/(1 + r),$$

where N is the original sample size, N_{eff} is the effective sample size, and r denotes lag 1 autocorrelation. Using this method, the effective sample sizes for the first three EOF modes of China summer HWs during the period of 1961–2015 ($N = 55$) are 16, 39, and 43, respectively. The statistical significance of the regression/correlation results is tested by the Student's t test based on the effective sample sizes.

3. Spatiotemporal characteristics and dominant modes of China HWD

a. Climatology, trends, and year-to-year variability of China HWs

Figure 1a presents the climatological pattern of JJA mean Tmax, which shows a south high–north low temperature landscape. The highest temperature appears in SC, which exceeds 32°C. The climatic Tmax in the northwestern region is as high as that in SC, due partly to the semiaridity and desert climate there (Wu et al. 2015). A moderate-high Tmax is found over central and eastern China ranging from 30° to 32°C, while the Tmax in northern and northeastern China is below 30°C. In comparison, Fig. 1b shows the 95th percentile thresholds of China HWs averaged in JJA. The spatial distribution of the 95th threshold is similar to the climatology of Tmax, where the largest thresholds appear in the southeastern and northwestern regions.

The climatology, linear trends, and standard deviations of HWD, calculated based on the 95th percentile threshold, are presented in Fig. 2. Unlike the spatial patterns of climatic Tmax, the largest HWD (Fig. 2a) appears over the YRV and northwestern China, rather than the SC, implying that the frequency of China summer HWs does not necessarily depend on the background temperatures. Figure 2b illustrates the linear trends of HWD, where significantly upward trends are observed in two regions: NC and the Pearl River Delta in SC. The maximum trend of HWD exceeds 6 days in 55 years (Fig. 2b), implying a dramatic increase in HW frequency. In comparison, the linear trends of HWD become small over the widespread areas of central and eastern China and even negative in some regions between the Yellow River and the Yangtze River, consistent with previous studies (Zhai et al. 1999). Moreover, Fig. 2c displays the variability of HWDs in terms of standard deviations and shows that the HWDs in NC, the YRV, and SC have relatively larger variances, suggesting stronger variations of HW frequency over these regions. It should be noted that the YRV and SC, which are the main hubs of China's fast economic growth, are densely urbanized and populated. Therefore, the frequent emergences of HWs over these regions may cause more severe impacts on the local society and economy.
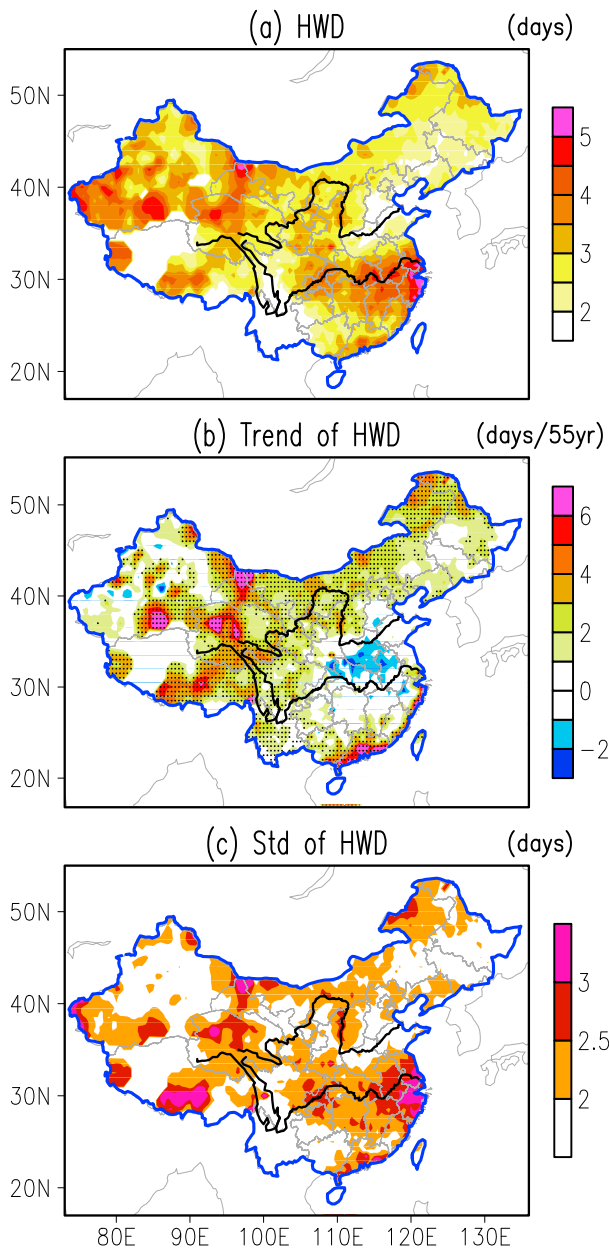
FIG. 2. (a) Climatology, (b) linear trends, and (c) standard deviations of JJA heat wave days (HWD), during the period of 1961–2015. Dotted areas in (b) indicate that the linear trends of HWD over these regions exceed the 95% confidence level.

b. Dominant modes of China HWs

To better understand the spatiotemporal characteristics of China summer HWs, we further investigate the dominant EOF modes of the HWs. As shown in Fig. 3, the first three leading modes of HWD account for 21.2%, 14.6%, and 8.4% of the total variances, respectively, which are statistically distinguishable from each other and from the remaining higher modes

according to the rule by North et al. (1982). The first three EOF modes of HWD show distinct spatial features that dominate in preferential regions.

As seen from Fig. 3a, the first mode of HWD reflects an increasing frequency of HWs across northwestern and northern China, covering Xinjiang, Gansu, Ningxia, and Inner Mongolia Provinces. Besides, such upward trends in HWD are also observed in Guangdong Province in SC. Figure 3b presents the time series corresponding to the first mode, which experienced a remarkable increasing trend since 1980s. The spatial pattern of the first mode matches the linear trends in HWD (see Fig. 2b) very well, which may result from the effects of global warming and/or multidecadal variability (Hu et al. 2017; Ren et al. 2017; Wang et al. 2017). Figure 3c presents the spatial pattern for the second mode, which reveals a strong variability of HWs in the YRV. Unlike the NC HWs that show an upward trend, the YRV HWs, captured by the second mode, mainly show interannual variations (Fig. 3d). Compared with the spatiotemporal features of the first mode, the HWs revealed by the second mode seem to concentrate preferentially in eastern China, with the strongest signals over the lower reaches of Yangtze River basin. Figure 3e depicts the spatial pattern for the third mode, which primarily reflects a strong interannual variability of HWs, although an interdecadal signal could also exist (Liu et al. 2015). The largest variances associated with the third mode of HWD mainly appear over SC, especially in the coastal provinces, such as Guangdong and Fujian Provinces. The most notable cases associated with the third mode of China HWD are the 1998 and 2003 HWs, which correspond to the 1997/98 and 2002/03 El Niño to La Niña transitions, respectively (e.g., Wang et al. 2013; Chen et al. 2016).

The 2010, 2013, and 1998/2003 summer HWs, as revealed by the first three EOF modes, are found to be the most prominent cases over NC, the YRV, and SC, respectively (see the right panels of Fig. 3). Thereby, Fig. 4 further scrutinizes the spatiotemporal variations of these cases for the comparison purposes. As shown in Fig. 4a, the largest values of 2010 summer HWD appear in the western and northern regions. Based on the record at Jiuquan station within a city in NC, the 2010 HWs broke out in early July and persisted to the end of this month, whose peak temperatures exceed 39°C, about 6°C above the threshold (Fig. 4b). However, the largest values of 2013 summer HWD are observed in eastern China (Fig. 4c). As an example, Fig. 4d depicts the time series of Tmax at the Shanghai station in eastern China during the 2013 summer. The 2013 Shanghai HWs seem to be more intense than the 2010 NC HWs, from the perspective of either relative thresholds or absolute
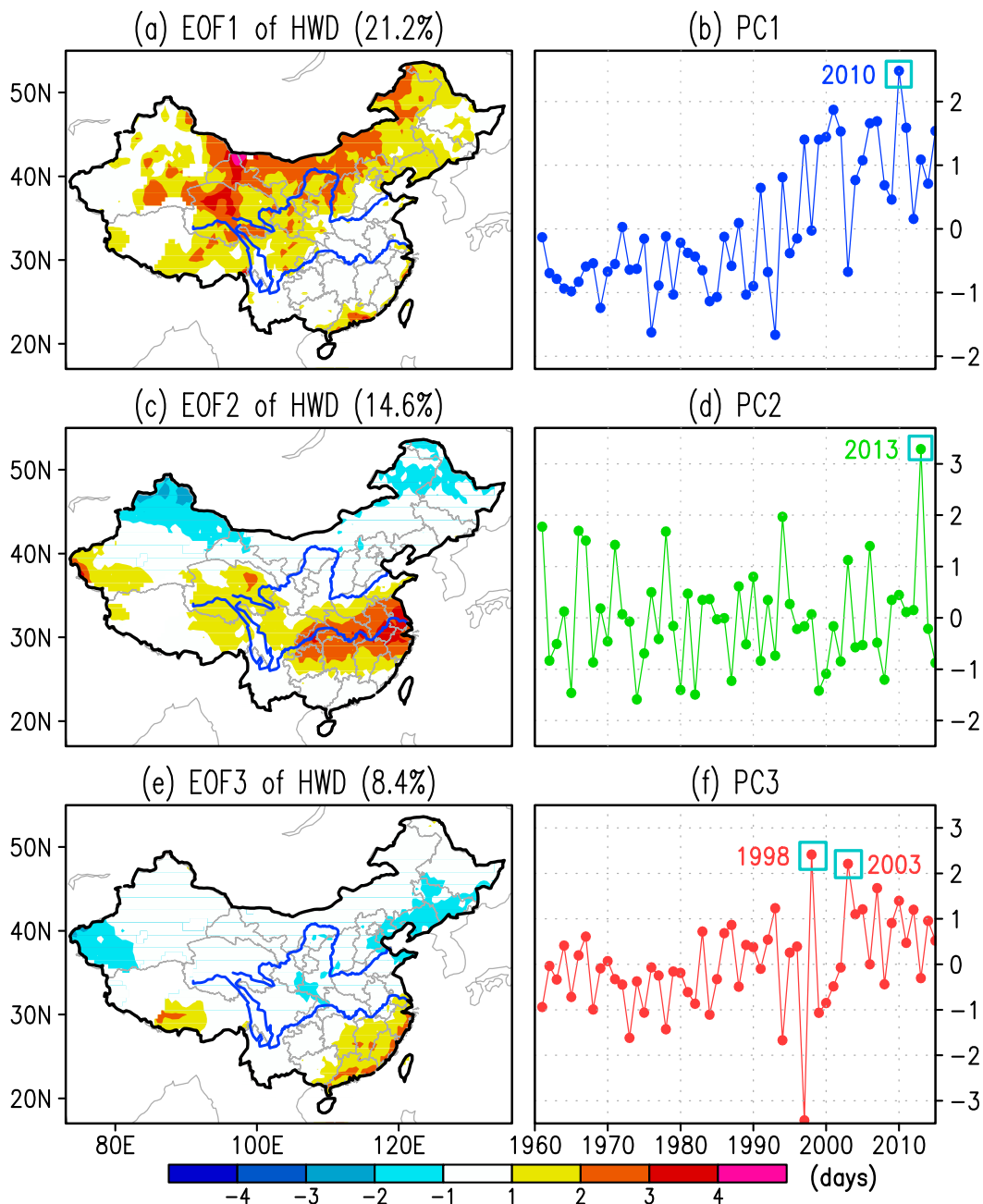
FIG. 3. (a),(c),(e) The spatial patterns for the first three EOF modes of China HWD, and (b),(d),(f) the corresponding time series.

temperatures; they occurred in late July and were sustained to 20 August, with a maximum temperature above 41°C and a HW amplitude over 3°C. Figure 4e shows the summer HWD in 2003, when the HWs primarily emerged in SC, which is similar to the spatial pattern for EOF3. We show, in Fig. 4f, the 2003 summer Tmax at Fuzhou station in SC, whose 95th percentile threshold is about 37°C, larger than that at the Jiuquan station but smaller than that at the Shanghai station.

Compared with the 2010 NC HWs and the 2013 YRV HWs, the 2003 HWs seem to show a longer duration, persisting throughout all of July and early August.

4. Drivers and mechanisms for the dominant modes of China HWs

Figure 5 presents the spatial patterns of sea level pressure (SLP), precipitation, and soil moisture correlated
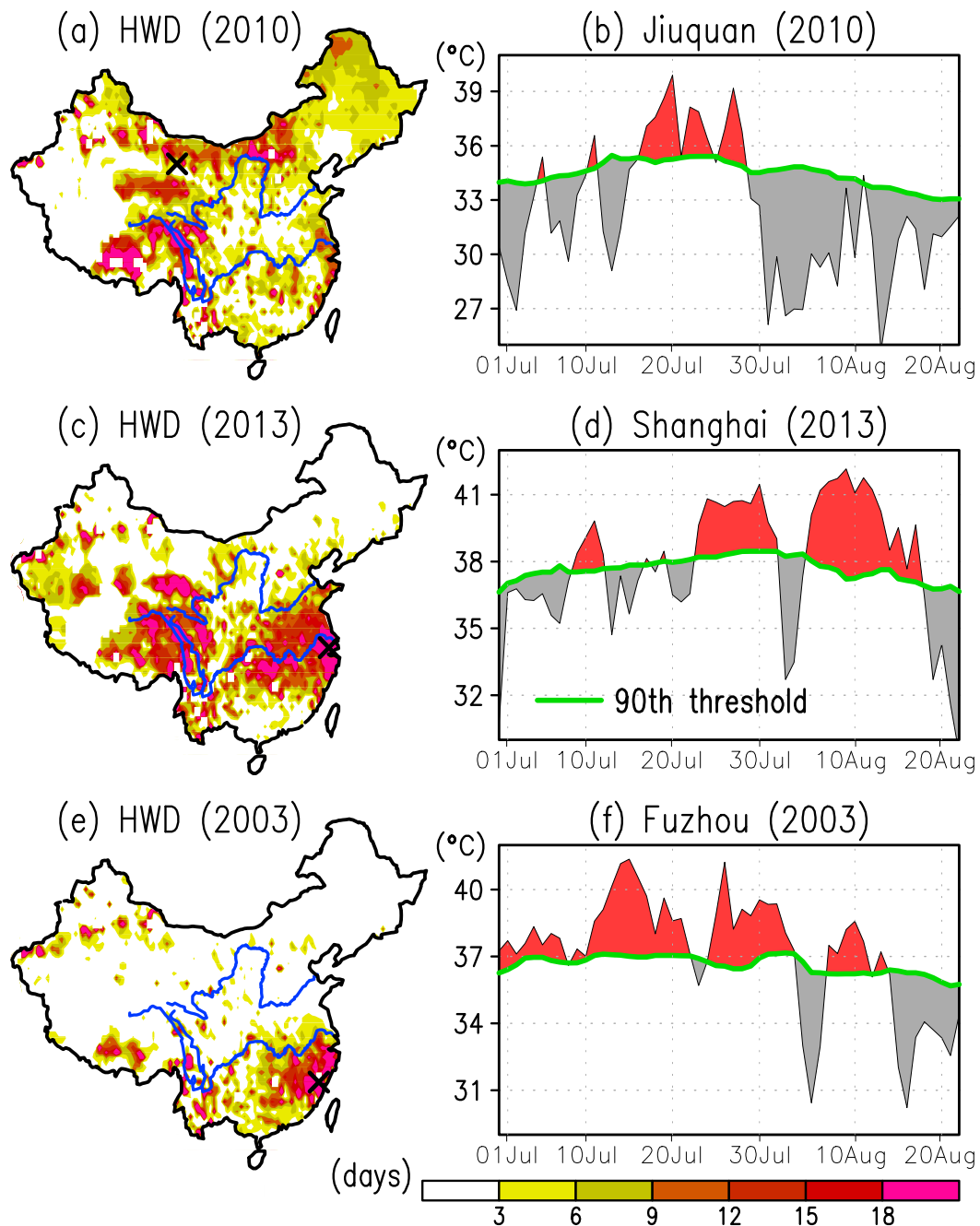
(a) HWD (2010)

(b) Jiuquan (2010)

(c) HWD (2013)

(d) Shanghai (2013)

90th threshold

(e) HWD (2003)

(f) Fuzhou (2003)

(days)

3 6 9 12 15 18

FIG. 4. (a),(c),(e) HWDs in 2010, 2013, and 2003, respectively. (b) Tmax at Jiuquan station (40°N, 98°E) during 2010 summer. (d),(f) As in (b), but for 2013 Shanghai station (30°N, 120°E) and 2003 Fuzhou station (26°N, 119°E), respectively.

with the PCs, in order to investigate the atmospheric circulations and soil conditions relevant to the dominant modes of China summer HWs. As seen from the upper panels of Fig. 5, the positive phases of the first three modes (i.e., more HWs in NC, the YRV, and SC) are significantly correlated with anomalously high SLPs over respective regions, where significantly decreased precipitation (middle panels) and reduced soil moisture (lower panels) are also observed. On the one hand, the clear skies due to anomalous high pressure will increase the solar radiation at the surface that heats the soil. The soil moisture has a season-long memory, whose signals can persist from antecedent spring to the following summer, which may act as a potential indicator for the
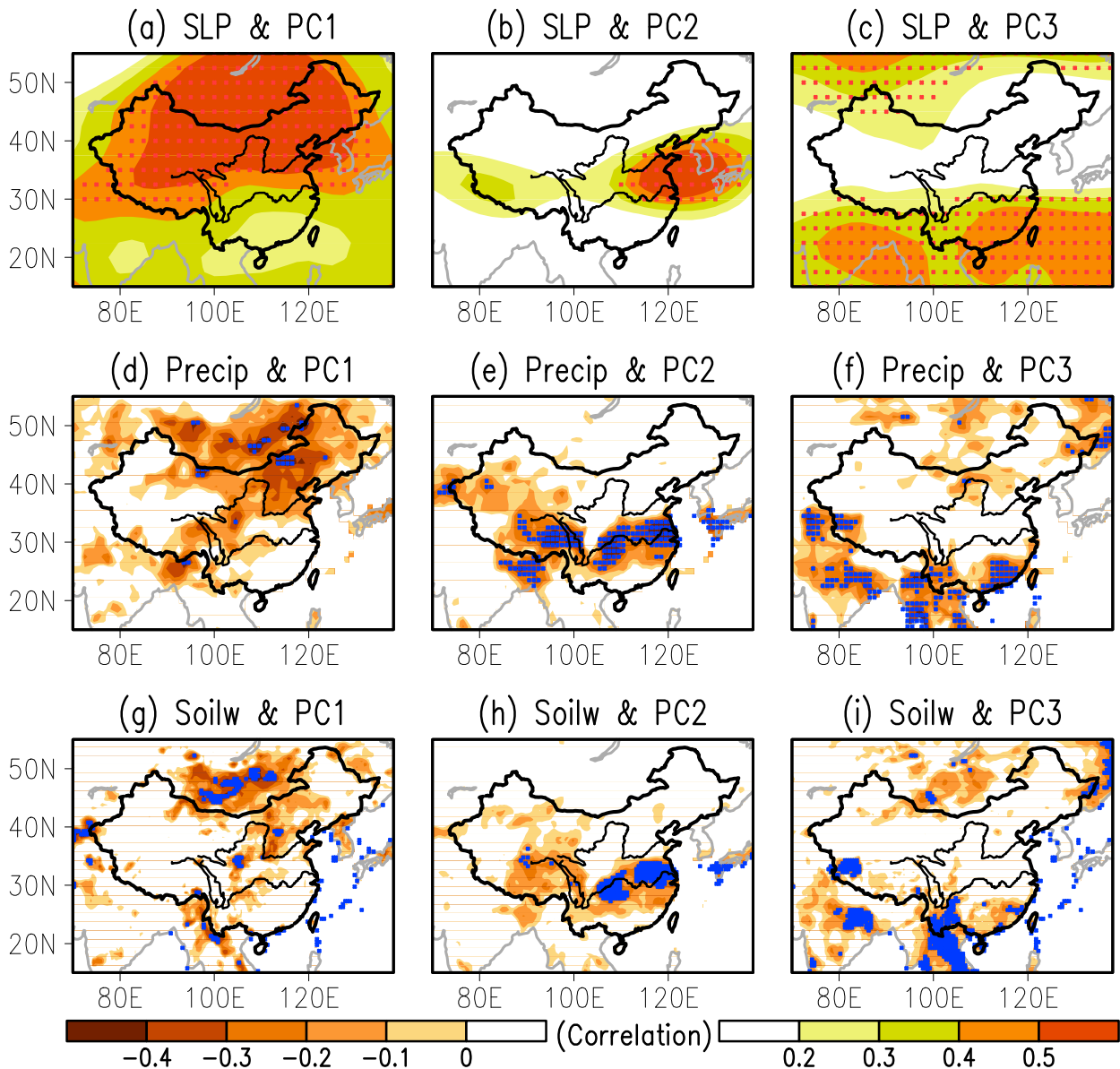
FIG. 5. Correlation maps of JJA (a)–(c) sea level pressure (SLP), (d)–(f) precipitation, and (g)–(i) subsurface soil moisture with (left) PC1, (middle) PC2, and (right) PC3. Dotted areas indicate that the correlation over these regions exceed the 90% confidence level. As the effective sample sizes for PC1, PC2, and PC3 are quite different (16, 39, and 43), we note that the thresholds of correlation coefficient exceeding the 90% confidence levels for the first three EOF modes are 0.42, 0.27, and 0.25, respectively.

seasonal prediction of China HWs. On the other hand, the lower rainfall–smaller evaporation feedbacks may lead to a drier soil condition. As a result, the surface temperature tends to increase, which favors the occurrences of HWs. We note that we have also examined the vertically integrated horizontal heat fluxes associated with the first three EOF modes (figure not shown), and find that the HWs over NC and the YRV are also likely to be affected by the horizontal heat fluxes. Thus, the anomalous atmospheric circulations over respective

regions may affect the regional HWs through not only the radiation fluxes but also the surface heat transport.

It is of great interest to explore why the anomalous highs, associated with the dominant modes of China HWs, appear over these regions. Figure 6 shows the regression maps of global SSTAs and atmospheric circulations against PC1. As seen from Fig. 6a, the increased frequency of NC HWs is significantly correlated with warm SSTs in the North Atlantic, the Indian Ocean, and the northwestern Pacific, which is
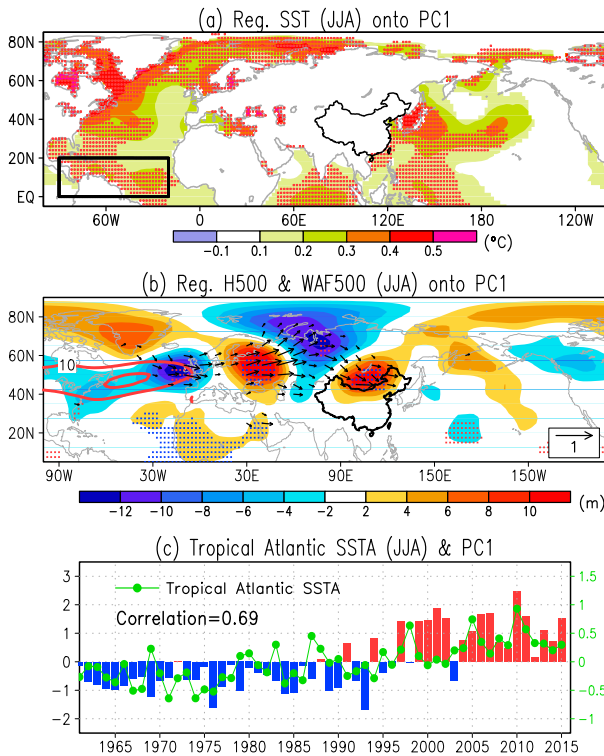
FIG. 6. Regression maps of (a) SSTA (unit: °C), and (b) H500 (unit: m) and Plumb's wave activity flux (unit: $m^2 s^{-2}$) onto the PC1. Stippled areas in (a) and (b) indicate the anomalies that exceed the 95% confidence levels, and contours in (b) denote the North Atlantic westerly jet stream at 500 hPa. Note that significant wave trains seem to originate over the subtropical eastern Atlantic. (c) PC1 (bar) and SSTA series (green curve) averaged over the subtropical Atlantic (0°–20°N, 90°–20°W) outlined by square box in (a).

reminiscent of the global warming signals or multidecadal variability (Knight et al. 2006). We note that the SSTAs in the North Atlantic and the North Pacific are more likely responses to the atmosphere rather than the forcing, as the SSTs in these regions are insufficient to trigger deep convection. Also, by examining the anomalously atmospheric circulation and wave activity fluxes, it is proposed that the Indian Ocean warm SSTAs should actually reflect the global warming signals, rather than a direct forcing to the atmosphere.

Figure 6b shows the regression pattern of 500-hPa geopotential height (H500) and Plumb's wave activity flux (Plumb 1985) onto PC1. As seen from Fig. 6b, significant high pressure anomalies appear over the subtropical eastern Atlantic, which are connected with alternatively negative and positive pressure centers over the North Atlantic and the Eurasian continent, with one propagating poleward and leading to an abnormal high over the Greenland island and the other propagating eastward and resulting in an anomalous anticyclone over

NC and the North Pacific. The anomalous anticyclones and high pressures over the high latitudes are often accompanied by descending air motion, reduced cloud cover, and increased solar radiation, which may cause the warm SSTAs in around Greenland and the North Pacific. An analysis of the wave activity flux indicates that the NC HWs could be linked to the tropical Atlantic warm SSTAs, which may trigger the zonally propagating wave trains. To explore the linkage between NC HWs and the tropical North Atlantic SSTs, we calculate the SSTA time series that is averaged over the domain of 0°–20°N, 90°–20°W. As shown in Fig. 6c, the tropical North Atlantic SSTAs experienced similar variations as the PC1, both of which underwent a decadal shift in the mid-1990s and reached peak intensity in 2010. The correlation coefficient between the tropical North Atlantic SST and PC1 is 0.69, which significantly exceeds the 95% confidence level. That is, the tropical Atlantic SSTs could play an important role in affecting the NC HWs.

It should be emphasized that the EOF1-related Rossby wave trains are different from the circumglobal teleconnection (CGT) pattern proposed by Ding and Wang (2005) in terms of wavenumbers, propagating routes, and locations of the centers of action. Actually, the wave trains displayed in Fig. 6a well resemble the summertime teleconnection, the North Atlantic–Eurasian (AEA) teleconnection. Li and Ruan (2018) have investigated the AEA teleconnection by statistical and dynamical analyses and discovered five centers of action in the subtropical North Atlantic, the northeastern North Atlantic, eastern Europe, the Kara Sea, and northern China, respectively. They addressed that the AEA underwent a high degree of year-to-year variability and exhibited an increasing trend over the last 30 years, consistent with the NC HWs. Based on the methods of stationary wave ray tracing, wave activity flux calculations, and numerical experiments, Li and Ruan (2018) further proposed that the AEA pattern could be possibly forced by the tropical North Atlantic SSTAs.

Figure 7a displays the regression map of global SSTAs against the second EOF mode of China HWs. Compared with the first mode, the second mode (i.e., variability in YRV HWs) seems to show insignificant correlation with SSTAs in most regions, although warm SSTAs are spotted in some areas of the North Atlantic and the North Pacific. Lee and Seo (2013) have showed that the SSTA forcing in the North Atlantic can generate an anticyclonic anomaly to the Korean peninsula, but the Atlantic SST–forced wave trains are more similar to those in EOF1, instead of those in Fig. 7b. As mentioned before, the SSTs in the mid- to high latitudes are too cold to trigger deep convection, so the warm SSTAs observed in these regions are believed to be
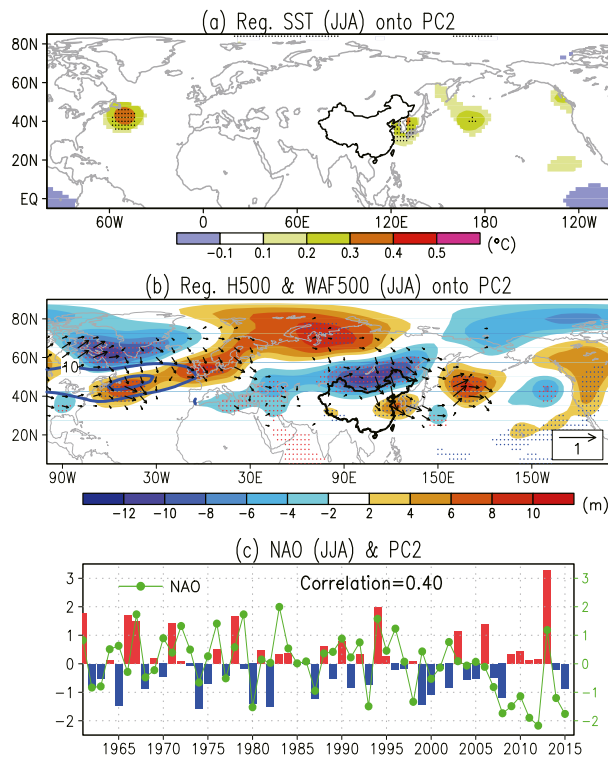
FIG. 7. (a),(b) As in Fig. 6, but for PC2. (c) PC2 (bar) and the North Atlantic Oscillation index (green curve) during the boreal summer.

responses to the atmosphere rather than a forcing. Further examination reveals that the second mode of China HWs may be affected by the atmospheric internal variability. As seen from Fig. 7b, the YRV HWs are significantly correlated with a dipole circulation pattern over the North Atlantic, where an anomalous high stretches northeastward from the North Atlantic to Europe and northern Russia while an anomalous low pressure locates to its north (60°–80°N). Moreover, an anomalous wave train is induced across East Asia, leading to an intensified anticyclone over the YRV. It is worth mentioning that the anomalous atmospheric circulation patterns are similar to the pattern induced by the North Atlantic Oscillation (NAO). The positive phase of NAO is featured by a low pressure anomaly that centers over the high-latitude North Atlantic at 60°–80°N and a high pressure anomaly over the 30°–60°N Atlantic regions (Ambaum et al. 2001), where the anomalous high pressure extends northeastward and further triggers a southeastward propagating wave train. Figure 7c presents the time series of PC2 and NAO, whose correlation coefficient during 1961–2015 is 0.4, which exceeds the 95% confidence level, suggesting that the NAO could be a major mode in the atmospheric internal variability that affects the YRV HWs.

Compared with the first two EOF modes, the oceanic drivers to the third mode of China HWD seem to be more apparent. As seen from the left panels of Fig. 8, the third mode of China HWs (i.e., variability in the SC HWs) is significantly correlated with the transition phase of El Niño to La Niña. During the preceding winter, warming SSTAs appear in the eastern Pacific, which gradually decay in the boreal spring and become insignificant in the concurrent summer. Meanwhile, the SSTAs in the Indian Ocean and the west Pacific increase gradually. Previous studies have discussed the physical mechanisms for how the eastern Pacific El Niño leads to the anomalous western Pacific anticyclone and subsequently affects East Asian climate, among which Xie et al. (2009) have emphasized the capacitor effect of the Indian Ocean. That is, the tropical Indian Ocean warming induced by previous El Niño could cause the local tropospheric temperature to increase by a moist-adiabatic adjustment in deep convection, which emanates a baroclinic Kelvin wave into the Pacific. In the northwest Pacific, this equatorial Kelvin wave may trigger suppressed convection and anomalous anticyclone. The right panels of Fig. 8 show the lagged regression of H500 against the PC3. During the preceding winter, anomalous low pressure exist over SC, where the anomalous low pressure weakens during the spring and switches to anomalous high pressure in summer. As indicated by Fig. 8g, the correlation coefficient between PC3 and the preceding DJF Niño-3.4 index is 0.42, significant exceeding the 99% confidence level. As the SC HWs are tied to the preceding El Niño, it is possible to improve the seasonal-to-interannual predictive skills for SC HWs based on ENSO.

The above analysis reveals that the variabilities in NC and SC HWs are associated with the Atlantic and the Pacific SSTAs, respectively, and the variability in YRV HWs tends to be modulated by the atmospheric internal variability (i.e., the NAO). To assess the model's performance in simulating the dominant modes of China HWs, we further analyze the data from HiRAM experiments. As seen from Fig. 9a, the first mode of HiRAM HWD is similar to that in observation, which is featured by an increased frequency of HWs in NC and shows significant correlation with the North Atlantic warm SSTAs. The second mode of HiRAM HWD reflects the El Niño–related mode in China HWs, with the largest variability centering in SC (Fig. 9c). In general, the GFDL HiRAM experiments are able to reproduce the historical evolution of NC and SC HWs, but fail to capture the variations of HWs in YRV. The correlation coefficient between model PC1 (PC2) and observed PC1 (PC3) for the period of 1979–2008 is 0.65 (0.38), which significantly exceeds
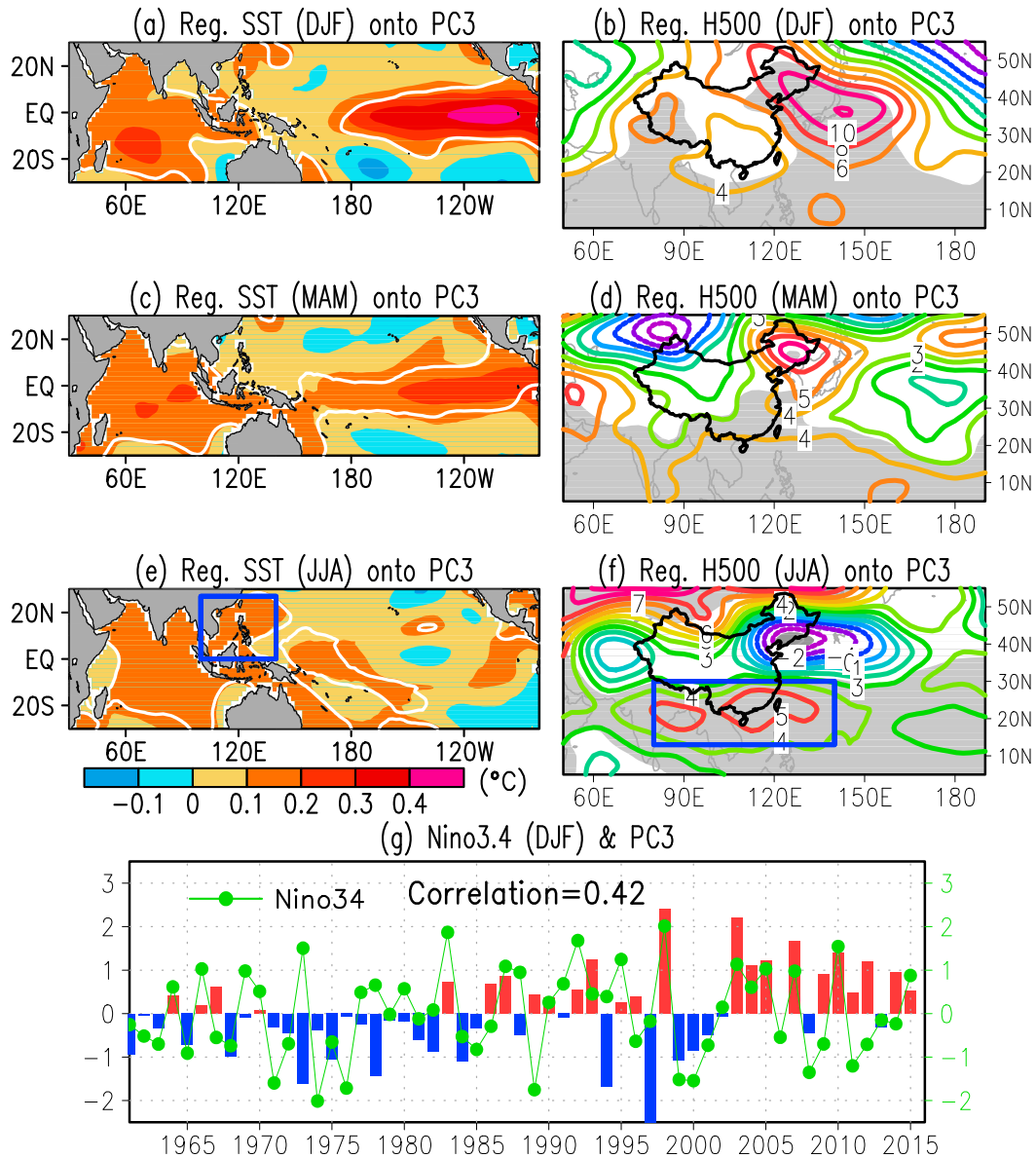
FIG. 8. (a)–(f) As in Fig. 6, but for the lagged regressions onto PC3. (g) PC3 (bar) and the preceding winter (DJF) Niño-3.4 index (green curve). Areas above the 95% confidence level for SST/H500 are marked by white contours (left)/shadings (right).

the 95% (90%) confidence level, indicating that this model has a more faithful representation of the SST-related modes of China HWs. Furthermore, Fig. 10 presents the regression maps of HiRAM H500 and WAF against the first two modes of HiRAM HWD. As seen from Fig. 10a, the zonally propagating wave trains, associated with the NC HWs, are well simulated, with a high pressure anomaly over the subtropical North Atlantic and a low pressure anomaly to its north, where the Rossby waves propagate eastward, leading to anomalous high pressure over NC. The

anomalous wave trains displayed in Fig. 10a is similar to the AEA pattern. Figure 10b presents the anomalous circulation pattern related to the SC HWs, where abnormal highs appear over SC during the boreal summer, which is consistent with the observed analysis in EOF3. It should be noted that our EOF analysis to the HiRAM simulation cannot extract HWD variability in the YRV as one of the leading modes. From the above analysis, it is suggested that the HiRAM should have a more faithful representation for the SST-related modes of China HWs.
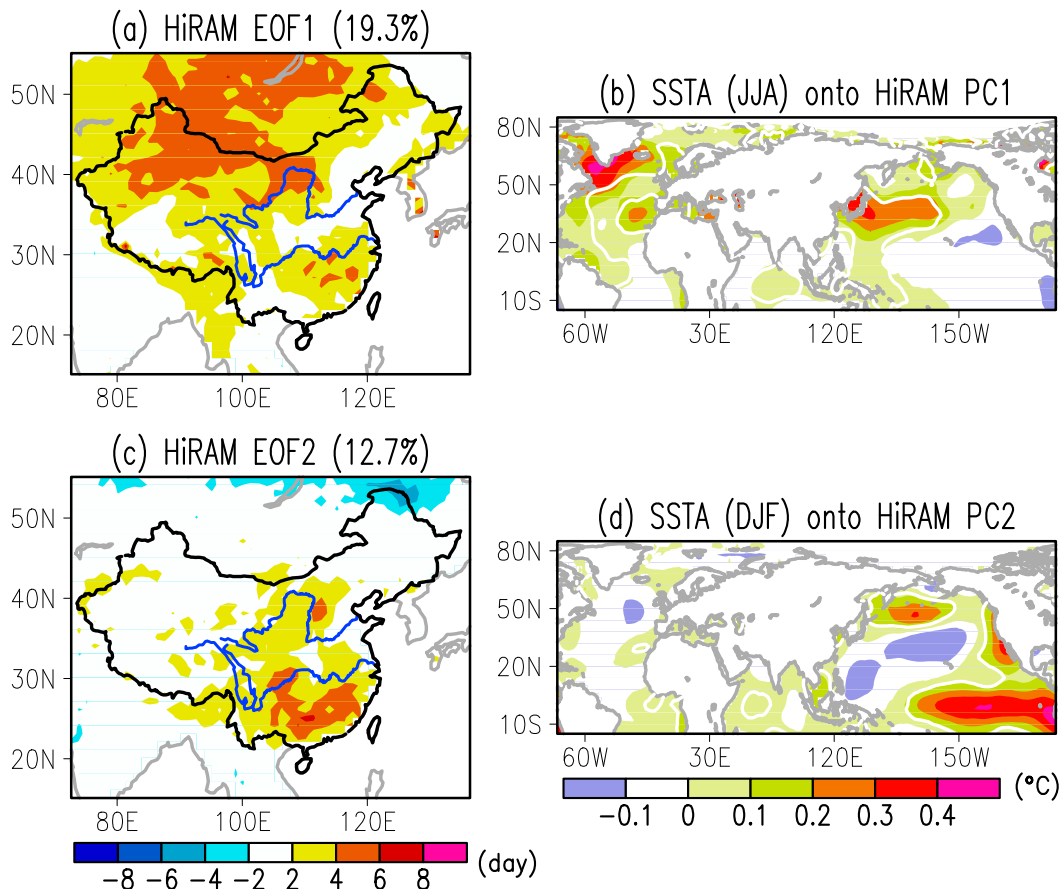
FIG. 9. (left) Spatial patterns for the (a) first and (c) second EOF modes of China summertime HWDs that are simulated by the high-resolution atmospheric model. (right) Regression maps of SSTAs onto the (b) PC1 and (d) PC2, where the areas exceeding the 95% confidence levels are outlined by white contours.

5. Summary and discussion

This study investigates the spatiotemporal characteristics of China summer HWs and explores the underlying mechanisms for the first three EOF modes of China HWD based on station and reanalysis datasets. It is found that the northern China (NC) HWs present an upward trend during the period of 1961–2015, but the Yangtze River valley (YRV) and southern China (SC) HWs mainly experience interannual variations. All of the first three modes of China HWs are associated with anomalous highs over respective regions, which are accompanied by reduced precipitation and increased solar radiation that cause a hotter and drier soil condition that favors the occurrence of HWs.

The first EOF mode of China HWD reflects an increased frequency of NC HWs, which shows a significant relationship with the Atlantic SST. The warm SSTAs in tropical North Atlantic may affect the NC HWs through the Atlantic–Eurasian teleconnection. That is, the

Atlantic-forced Rossby wave trains propagate eastward and lead to an intensified anticyclone over NC. The second EOF mode of China HWD reveals the interannual variability in YRV HWs, which is believed to be connected with the NAO. The positive phases of NAO correspond to a dipole circulation pattern over the Atlantic, where the anomalous high pressure stretches northeastward from the North Atlantic to northern Russia, subsequently inducing a southeastward propagating wave train over East Asia and causing anomalous anticyclones over the YRV. The third EOF mode of China HWD reflects the interannual variability in SC HWs, which is dominated by the transition phase of El Niño to La Niña. The decay of eastern Pacific winter warming is accompanied by gradually warming in the Indian Ocean and the west Pacific during the boreal spring and summer, which eventually cause abnormal anticyclones over SC. We have also assessed the performance of GFDL HiRAM in simulating the dominant modes of China HWs. The HiRAM experiments have
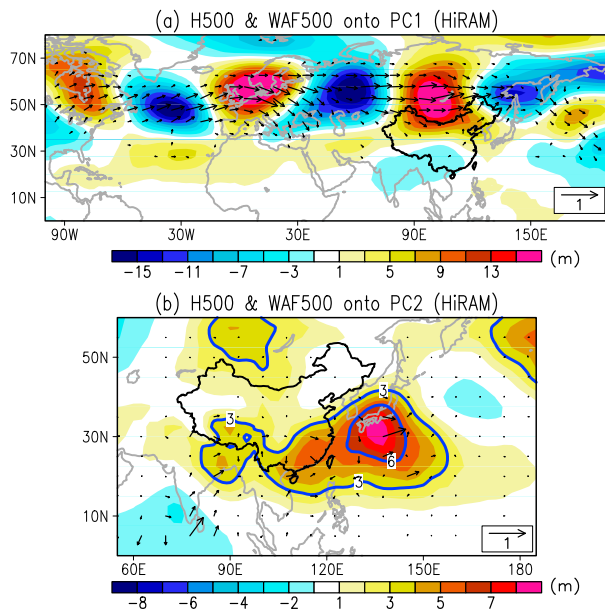
FIG. 10. Regression maps of model simulated H500 (shading; m) and Plumb's wave activity flux (vector; $m^2 s^{-2}$) onto (a) PC1 and (b) PC2.

well simulated the variability of HWs in NC and SC, but fail to capture the variability of YRV HWs, suggesting that the model has a better representation of the SST-related modes of China HWs than that forced by the atmospheric internal variability.

This study emphasizes the importance of oceanic and atmospheric drivers for the dominant modes of China HWs. The first and third modes of China HWD could be associated with the oceanic drivers, while the second mode of China HWD (i.e., variability in the YRV HWs) is affected by the atmospheric internal variability, especially the NAO. In addition, as the skill of model simulation of YRV HWs is limited, constructing a statistical model using the oceanic and atmospheric predictors, such as those proposed by Lee and Seo (2013), could be an alternative method for improving the forecast of YRV HWs. Finally, it should be cautioned that, in addition to the dominant modes in SST and atmospheric internal variability, the HWD can possibly be a direct response to external forcings such as the greenhouse gases and vegetation and land use changes. In particular, EOF1 of HWD, which shows an apparent upward trend, is more likely affected by these external forcings. Actually, Kang and Eltahir (2018) have projected based on an ensemble of high-resolution regional climate model simulations that climate change would add significantly to the anthropogenic effects of irrigation, which could increase the risk from the deadly heatwaves in northern China. That is, in the real world, HWs are affected by both the natural

modes in oceans and the atmosphere and the anthropogenic forcing, which have been extensively discussed in previous studies.

REFERENCES

Ambaum, M. H. P., B. J. Hoskins, and D. B. Stephenson, 2001: Arctic Oscillation or North Atlantic Oscillation? *J. Climate*, **14**, 3495–3507, https://doi.org/10.1175/1520-0442(2001) 014<3495:AOONAO>2.0.CO;2.

Barriopedro, D., E. M. Fischer, J. Luterbacher, R. M. Trigo, and R. García-Herrera, 2011: The hot summer of 2010: Redrawing the temperature record map of Europe. *Science*, **332**, 220–224, https://doi.org/10.1126/science.1201224.

Cao, L. J., Y. N. Zhu, G. L. Tang, F. Yuan, and Z. W. Yan, 2016: Climatic warming in China according to a homogenized data set from 2419 stations. *Int. J. Climatol.*, **36**, 4384–4392, https://doi.org/10.1002/joc.4639.

Chen, R., and R. Lu, 2015: Comparisons of the circulation anomalies associated with heat in different regions of eastern China. *J. Climate*, **28**, 5830–5844, https://doi.org/10.1175/JCLI-D-14-00818.1.

——, Z. Wen, and R. Lu, 2016: Evolution of the circulation anomalies and the quasi-biweekly oscillations associated with extreme heat events in southern China. *J. Climate*, **29**, 6909–6921, https://doi.org/10.1175/JCLI-D-16-0160.1.

——, ——, and ——, 2018: Large-scale circulation anomalies and intraseasonal oscillations associated with long-lived extreme heat events in South China. *J. Climate*, **31**, 213–232, https://doi.org/10.1175/JCLI-D-17-0232.1.

Chen, Y., and P. Zhai, 2017: Simultaneous modulations of precipitation and temperature extremes in southern parts of China by the boreal summer intraseasonal oscillation. *Climate Dyn.*, **49**, 3363–3381, https://doi.org/10.1007/s00382-016-3518-4.

Coumou, D., and S. Rahmstorf, 2012: A decade of weather extremes. *Nat. Climate Change*, **2**, 491–496, https://doi.org/10.1038/nclimate1452.

Cressman, G. P., 1959: An operational objective analysis system. *Mon. Wea. Rev.*, **87**, 367–374, https://doi.org/10.1175/1520-0493(1959)087<0367:AOOAS>2.0.CO;2.

Della-Marta, P. M., J. Luterbacher, H. von Weissenfluh, E. Xoplaki, M. Brunet, and H. Wanner, 2007: Summer heat waves over western Europe 1880–2003, their relationship to large-scale forcings and predictability. *Climate Dyn.*, **29**, 251–275, https://doi.org/10.1007/s00382-007-0233-1.

Deng, K. Q., S. Yang, M. Ting, Y. Tan, and S. He, 2018a: Global monsoon precipitation: Trends, leading modes, and associated drought and heat wave in the Northern Hemisphere. *J. Climate*, **31**, 6947–6966, https://doi.org/10.1175/JCLI-D-17-0569.1.

——, M. Ting, S. Yang, and Y. Tan, 2018b: Increased frequency of summer extreme heat waves over Texas area tied to the amplification of Pacific zonal SST gradient. *J. Climate*, **31**, 5629–5647, https://doi.org/10.1175/JCLI-D-17-0554.1.

Ding, Q. H., and B. Wang, 2005: Circumglobal teleconnection in the Northern Hemisphere summer. *J. Climate*, **18**, 3483–3505, https://doi.org/10.1175/JCLI3473.1.

Ding, T., W. Qian, and Z. Yan, 2010: Changes in hot days and heat waves in China during 1961–2007. *Int. J. Climatol.*, **30**, 1452–1462, https://doi.org/10.1002/joc.1989.

Dole, R., and Coauthors, 2011: Was there a basis for anticipating the 2010 Russian heat wave? *Geophys. Res. Lett.*, **38**, L06702, https://doi.org/10.1029/2010GL046582.

Fischer, E. M., S. I. Seneviratne, P. L. Vidale, D. Lüthi, and C. Schär, 2007: Soil moisture–atmosphere interactions during the 2003 European summer heatwave. *J. Climate*, **20**, 5081–5099, https://doi.org/10.1175/JCLI4288.1.

Fouillet, A., and Coauthors, 2006: Excess mortality related to the August 2003 heat wave in France. *Int. Arch. Occup. Environ. Health*, **80**, 16–24, https://doi.org/10.1007/s00420-006-0089-4.

Gu, S., C. Huang, L. Bai, C. Chu, and Q. Liu, 2016: Heat-related illness in China, summer of 2013. *Int. J. Biometeor.*, **60**, 131–137, https://doi.org/10.1007/s00484-015-1011-0.

Guo, X., J. Huang, Y. Luo, Z. Zhao, and Y. Xu, 2017: Projection of heat waves over China for eight different global warming targets using 12 CMIP5 models. *Theor. Appl. Climatol.*, **128**, 507–522, https://doi.org/10.1007/s00704-015-1718-1.

Harris, L. M., S.-J. Lin, and C. Y. Tu, 2016: High-resolution climate simulations using GFDL HiRAM with a stretched global grid. *J. Climate*, **29**, 4293–4314, https://doi.org/10.1175/JCLI-D-15-0389.1.

Hirschi, M., and Coauthors, 2011: Observational evidence for soil-moisture impact on hot extremes in southeastern Europe. *Nat. Geosci.*, **4**, 17–21, https://doi.org/10.1038/ngeo1032.

Hu, K., G. Huang, X. Qu, and R. Huang, 2012: The impact of Indian Ocean variability on high temperature extremes across the southern Yangtze River valley in late summer. *Adv. Atmos. Sci.*, **29**, 91–100, https://doi.org/10.1007/s00376-011-0209-2.

Hu, L. S., G. Huang, and X. Qu, 2017: Spatial and temporal features of summer extreme temperature over China during 1960–2013. *Theor. Appl. Climatol.*, **128**, 821–833, https://doi.org/10.1007/s00704-016-1741-x.

Huang, B., and Coauthors, 2015: Extended reconstructed sea surface temperature version 4 (ERSST.v4). Part I: Upgrades and intercomparisons. *J. Climate*, **28**, 911–930, https://doi.org/10.1175/JCLI-D-14-00006.1.

Kalnay, E., and Coauthors, 1996: The NCEP/NCAR 40-Year Reanalysis Project. *Bull. Amer. Meteor. Soc.*, **77**, 437–471, https://doi.org/10.1175/1520-0477(1996)077<0437:TNYRP>2.0.CO;2.

Kang, S., and E. A. Eltahir, 2018: North China Plain threatened by deadly heatwaves due to climate change and irrigation. *Nat. Commun.*, **9**, 2894, https://doi.org/10.1038/s41467-018-05252-y.

Knight, J. R., C. K. Folland, and A. A. Scaife, 2006: Climatic impacts of the Atlantic multidecadal oscillation. *Geophys. Res. Lett.*, **33**, L17706, https://doi.org/10.1029/2006GL026242.

Konovalov, I., M. Beekmann, I. Kuznetsova, A. Yurova, and A. Zvyagintsev, 2011: Atmospheric impacts of the 2010 Russian wildfires: Integrating modelling and measurements of an extreme air pollution episode in the Moscow region. *Atmos. Chem. Phys.*, **11**, 10 031–10 056, https://doi.org/10.5194/acp-11-10031-2011.

Kuglitsch, F. G., A. Toreti, E. Xoplaki, P. M. Della-Marta, C. S. Zerefos, M. Türkeş, and J. Luterbacher, 2010: Heat wave changes in the eastern Mediterranean since 1960. *Geophys. Res. Lett.*, **37**, L04802, https://doi.org/10.1029/2009GL041841.

Lee, S.-S., and K.-H. Seo, 2013: The development of a statistical forecast model for changma. *Wea. Forecasting*, **28**, 1304–1321, https://doi.org/10.1175/WAF-D-13-00003.1.

Li, J. P., and C. Q. Ruan, 2018: The North Atlantic–Eurasian teleconnection in summer and its effects on Eurasian climates. *Environ. Res. Lett.*, **13**, 024007, https://doi.org/10.1088/1748-9326/aa9d33.

Liu, G., R. Wu, S. Sun, and H. Wang, 2015: Synergistic contribution of precipitation anomalies over northwestern India and the South China Sea to high temperature over the Yangtze River valley. *Adv. Atmos. Sci.*, **32**, 1255–1265, https://doi.org/10.1007/s00376-015-4280-y.

Luo, M., and N. C. Lau, 2017: Heat waves in southern China: Synoptic behavior, long-term change, and urbanization effects. *J. Climate*, **30**, 703–720, https://doi.org/10.1175/JCLI-D-16-0269.1.

Meehl, G. A., and C. Tebaldi, 2004: More intense, more frequent, and longer lasting heat waves in the 21st century. *Science*, **305**, 994–997, https://doi.org/10.1126/science.1098704.

Metz, W., 1991: Optimal relationship of large-scale flow patterns and the barotropic feedback due to high-frequency eddies. *J. Atmos. Sci.*, **48**, 1141–1159, https://doi.org/10.1175/1520-0469(1991)048<1141:OROLSF>2.0.CO;2.

North, G. R., T. L. Bell, R. F. Cahalan, and F. J. Moeng, 1982: Sampling errors in the estimation of empirical orthogonal functions. *Mon. Wea. Rev.*, **110**, 699–706, https://doi.org/10.1175/1520-0493(1982)110<0699:SEITEO>2.0.CO;2.

Perkins, S. E., and L. V. Alexander, 2013: On the measurement of heat waves. *J. Climate*, **26**, 4500–4517, https://doi.org/10.1175/JCLI-D-12-00383.1.

Plumb, R. A., 1985: On the three-dimensional propagation of stationary waves. *J. Atmos. Sci.*, **42**, 217–229, https://doi.org/10.1175/1520-0469(1985)042<0217:OTTDPO>2.0.CO;2.

Qian, W., 2017: Heat waves and cold events. *Temporal Climatology and Anomalous Weather Analysis*, Springer, 347–423, https://doi.org/10.1007/978-981-10-3641-5_7.

——, T. Yu, and J. Du, 2016: A unified approach to trace surface heat and cold events by using height anomaly. *Climate Dyn.*, **46**, 1647–1664, https://doi.org/10.1007/s00382-015-2666-2.

Ren, G., Y. Ding, and G. Tang, 2017: An overview of mainland China temperature change research. *J. Meteor. Res.*, **31**, 3–16, https://doi.org/10.1007/s13351-017-6195-2.

Rey, G., A. Fouillet, P. Bessemoulin, P. Frayssinet, A. Dufour, E. Jougla, and D. Hémon, 2009: Heat exposure and socioeconomic vulnerability as synergistic factors in heat-wave-related mortality. *Eur. J. Epidemiol.*, **24**, 495–502, https://doi.org/10.1007/s10654-009-9374-3.

Robinson, P. J., 2001: On the definition of a heat wave. *J. Appl. Meteor.*, **40**, 762–775, https://doi.org/10.1175/1520-0450(2001)040<0762:OTDOAH>2.0.CO;2.

Schneider, U., A. Becker, P. Finger, A. Meyer-Christoffer, M. Ziese, and B. Rudolf, 2014: GPCC's new land surface precipitation climatology based on quality-controlled in situ data and its role in quantifying the global water cycle. *Theor. Appl. Climatol.*, **115**, 15–40, https://doi.org/10.1007/s00704-013-0860-x.

Seo, K.-H., J.-H. Son, J.-Y. Lee, and H.-S. Park, 2015: Northern East Asian monsoon precipitation revealed by airmass variability and its prediction. *J. Climate*, **28**, 6221–6233, https://doi.org/10.1175/JCLI-D-14-00526.1.

Stéfanon, M., P. Drobinski, F. D'Andrea, C. Lebeaupin-Brossier, and S. Bastin, 2014: Soil moisture–temperature feedbacks at meso-scale during summer heat waves over Western Europe. *Climate Dyn.*, **42**, 1309–1324, https://doi.org/10.1007/s00382-013-1794-9.

Sun, Y., X. Zhang, F. W. Zwiers, L. Song, H. Wan, T. Hu, H. Yin, and G. Ren, 2014: Rapid increase in the risk of extreme summer heat in Eastern China. *Nat. Climate Change*, **4**, 1082–1085, https://doi.org/10.1038/nclimate2410.

Tan, J. G., Y. Zheng, G. Song, L. S. Kalkstein, A. J. Kalkstein, and X. Tang, 2007: Heat wave impacts on mortality in Shanghai, 1998 and 2003. *Int. J. Biometeor.*, **51**, 193–200, https://doi.org/10.1007/s00484-006-0058-3.

Wang, P., J. Tang, X. Sun, S. Wang, J. Wu, X. Dong, and J. Fang, 2017: Heat waves in China: Definitions, leading patterns, and connections to large-scale atmospheric circulation and SSTs. *J. Geophys. Res.*, **122**, 10 679–10 699, https://doi.org/10.1002/2017JD027180.

——, ——, S. Wang, X. Dong, and J. Fang, 2018: Regional heatwaves in China: A cluster analysis. *Climate Dyn.*, **50**, 1901–1917, https://doi.org/10.1007/s00382-017-3728-4.

Wang, W., W. Zhou, X. Wang, S. K. Fong, and K. C. Leong, 2013: Summer high temperature extremes in Southeast China associated with the East Asian jet stream and circumglobal teleconnection. *J. Geophys. Res.*, **118**, 8306–8319, https://doi.org/10.1002/jgrd.50633.

——, ——, X. Li, X. Wang, and D. Wang, 2016: Synoptic-scale characteristics and atmospheric controls of summer heat waves in China. *Climate Dyn.*, **46**, 2923–2941, https://doi.org/10.1007/s00382-015-2741-8.

Witte, J. C., A. R. Douglass, A. da Silva, O. Torres, R. Levy, and B. N. Duncan, 2011: NASA A-Train and Terra observations of the 2010 Russian wildfires. *Atmos. Chem. Phys.*, **11**, 9287–9301, https://doi.org/10.5194/acp-11-9287-2011.

Wu, Y., B. Bake, J. Zhang, and H. Rasulov, 2015: Spatio-temporal patterns of drought in North Xinjiang, China, 1961–2012 based on meteorological drought index. *J. Arid Land*, **7**, 527–543, https://doi.org/10.1007/s40333-015-0125-x.

Wu, Z., Z. Jiang, J. Li, S. Zhong, and L. Wang, 2012: Possible association of the western Tibetan Plateau snow cover with the decadal to interdecadal variations of northern China heatwave frequency. *Climate Dyn.*, **39**, 2393–2402, https://doi.org/10.1007/s00382-012-1439-4.

——, P. Zhang, H. Chen, and Y. Li, 2016: Can the Tibetan Plateau snow cover influence the interannual variations of Eurasian heat wave frequency? *Climate Dyn.*, **46**, 3405–3417, https://doi.org/10.1007/s00382-015-2775-y.

Xia, Y., and Coauthors, 2018: Assessment of the economic impacts of heat waves: A case study of Nanjing, China. *J. Clean. Prod.*, **171**, 811–819, https://doi.org/10.1016/j.jclepro.2017.10.069.

Xie, S.-P., K. Hu, J. Hafner, H. Tokinaga, Y. Du, G. Huang, and T. Sampe, 2009: Indian Ocean capacitor effect on Indo-western Pacific climate during the summer following El Niño. *J. Climate*, **22**, 730–747, https://doi.org/10.1175/2008JCLI2544.1.

Yang, J., H. Z. Liu, C. Q. Ou, G. Z. Lin, Y. Ding, Q. Zhou, J. C. Shen, and P. Y. Chen, 2013: Impact of heat wave in 2005 on mortality in Guangzhou, China. *Biomed. Environ. Sci.*, **26**, 647–654, https://doi.org/10.3967/0895-3988.2013.08.003.

Zhai, P., A. Sun, F. Ren, X. Liu, B. Gao, and Q. Zhang, 1999: Changes of climate extremes in China. *Climatic Change*, **42**, 203–218, https://doi.org/10.1023/A:1005428602279.

Zhang, L.-S.., J.-J. Xue, W.-G. Wang, and J. Sun, 2014: Comparative analysis of extreme high temperature weather in the summers of 2013 and 2003. *Atmos. Oceanic Sci. Lett.*, **7**, 132–136, https://doi.org/10.3878/j.issn.1674-2834.13.0073.

Zhang, Y., R. Feng, R. Wu, P. Zhong, X. Tan, K. Wu, and L. Ma, 2017: Global climatic change: Impact of heat waves under different definitions on daily mortality in Wuhan, China. *Global Health Res. Policy*, **2**, 10, https://doi.org/10.1186/s41256-017-0030-2.

Zhao, M., I. M. Held, S.-J. Lin, and G. A. Vecchi, 2009: Simulations of global hurricane climatology, interannual variability, and response to global warming using a 50-km resolution GCM. *J. Climate*, **22**, 6653–6678, https://doi.org/10.1175/2009JCLI3049.1.

Zhou, Y., and Z. Wu, 2016: Possible impacts of mega-El Niño/Southern Oscillation and Atlantic Multidecadal Oscillation on Eurasian heatwave frequency variability. *Quart. J. Roy. Meteor. Soc.*, **142**, 1647–1661, https://doi.org/10.1002/qj.2759.

Zwiers, F. W., and H. von Storch, 1995: Taking serial correlation into account in tests of the mean. *J. Climate*, **8**, 336–351, https://doi.org/10.1175/1520-0442(1995)008<0336:TSCIAI>2.0.CO;2.